

Article

Comparative Study of Magnet Temperature Estimation at Low Speeds Based on High-Frequency Resistance and Inductance

Hwigon Kim ¹, Seon-Gu Kang ², Jae-Jung Jung ³ and Hyun-Sam Jung ^{2,*}

¹ School of Electrical Engineering and Computer Science, Seoul National University, Seoul 08826, Republic of Korea

² Department of Electronics and Electrical Engineering, Dongguk University, Seoul 04620, Republic of Korea

³ Department of Electronic and Electrical Engineering, Kyungpook National University, Bukgu, Daegu 41566, Republic of Korea

* Correspondence: junghyunsam@dongguk.edu

Abstract: Interior permanent magnet synchronous motors have been widely used in electric vehicles. These motors employ Nd-Fe-B as the permanent magnet, which is vulnerable to temperature variations. Moreover, some features of Nd-Fe-B magnets are related to temperature, which can affect motor characteristics. Therefore, magnet temperature is an important parameter and methods for estimating it have been developed. In particular, a signal injection method has been developed for low-speed regions. In this method, two parameters are employed: high-frequency resistance and high-frequency inductance. In this paper, these two methods are compared to determine which parameter is more appropriate for estimations at low speeds and to reveal whether signal injection methods can be applied to the standstill condition. The comparison indicated that the high-frequency inductance-based method has a stronger correlation with the magnet temperature at low speed and standstill conditions than the high-frequency resistance-based method.

Keywords: motor drive; magnet temperature; high-frequency injection; magnet temperature estimation



Citation: Kim, H.; Kang, S.-G.; Jung, J.-J.; Jung, H.-S. Comparative Study of Magnet Temperature Estimation at Low Speeds Based on High-Frequency Resistance and Inductance. *Electronics* **2023**, *12*, 2011. <https://doi.org/10.3390/electronics12092011>

Academic Editor: Ibrahim Mohd Alsofyani

Received: 4 April 2023

Revised: 24 April 2023

Accepted: 24 April 2023

Published: 26 April 2023



Copyright: © 2023 by the authors. Licensee MDPI, Basel, Switzerland. This article is an open access article distributed under the terms and conditions of the Creative Commons Attribution (CC BY) license (<https://creativecommons.org/licenses/by/4.0/>).

1. Introduction

Recently, transportation has been electrified and the market for electric vehicles (EVs) is increasing. EVs have widely employed interior permanent magnet synchronous machines (IPMSMs) as traction motors, which typically use Nd-Fe-B as the permanent magnet. However, Nd-Fe-B is vulnerable to temperature variations because its residual flux density and intrinsic coercivity decrease with increasing magnet temperature, as shown in (1) [1]. These features can influence the characteristics of IPMSMs [2–4]. In particular, torque is directly affected by variations in residual flux density. Furthermore, rising magnet temperature makes the intrinsic coercivity decrease, which results in the magnet being much more prone to demagnetization [1,5].

$$\begin{aligned} B_r &= B_{r0}(1 + \alpha_{mag}(T_{mag} - 20)), \text{ and} \\ H_{ci} &= H_{ci0}(1 + \beta_{mag}(T_{mag} - 20)). \end{aligned} \quad (1)$$

Several studies have been conducted to monitor the magnet temperature using temperature sensors, such as platinum resistance temperature sensors, thermocouples, and infrared temperature sensors [6]. However, these measurements require modification of the motor's structure, which is not compatible with mass-produced traction motors. Therefore, methods for estimating the magnet temperature have been researched and developed. Generally, thermal models have been exploited to estimate the magnet temperature [7–10]. However, thermal models are complex and require knowledge regarding the environment, such as mechanical systems, cooling systems, and materials. Electrical models have also

been utilized to estimate the magnet temperature. These electrical model-based estimation methods can be classified into two types according to operating speed. Estimation methods in the medium- and high-speed regions exploit magnet flux linkage [11–15] or reactive energy [16–19], respectively. However, these methods cannot be applied where the motor's terminal voltages are insufficient due to operating at low speed. Therefore, an additional signal is injected [20–29], which can either be a pulse voltage [20,21] or a high-frequency (HF) sinusoidal signal [22–29]. The method in [20,21] injects a pulse voltage at a particular angle, which requires multisampling and DC injection at the d -axis; hence, it is difficult to apply to traction motor drives. The sinusoidal signal injection method was developed in [22–29]. In [22,23], HF resistance was obtained by injecting a sinusoidal voltage or current. The HF resistance includes the stator winding resistance. Therefore, by using measured stator winding temperature, the stator winding resistance component was eliminated. The study in [22,23] reported that the HF resistance after eliminating the stator winding resistance component varied according to the magnet temperature. In [24–29], the HF inductance was exploited to estimate magnet temperature, because HF inductance increases with the magnet temperature. This method does not require stator winding information, unlike the HF resistance-based method.

In this study, the HF resistance-based and HF inductance-based methods were compared. For this comparison, the HF resistance and HF inductance were extracted according to the torque and speed in a special rig, where the temperatures of the magnet and stator winding could be measured. From the extracted HF resistance and HF inductance, an analysis was conducted to determine which parameter was more appropriate for estimating the magnet temperature in low-speed regions. Additionally, it was determined whether the HF resistance-based and HF inductance-based methods could be applied in standstill conditions.

2. HF Resistance- and HF Inductance-Based Estimation Methods

An IPMSM model in the rotor reference frame is described in (2), where v , i , and λ are the voltage, current, and flux linkage, respectively. The superscript ' r ' in (2) refers to the rotor reference frame. R_s in (2) is the stator winding resistance, which varies with the stator winding temperature (T_{sw}). In (3), R_{s20} and α_{20} represent the stator winding resistance at $T_{sw} = 20^\circ\text{C}$ and the temperature coefficient of the winding material, respectively.

$$\begin{aligned} v_{ds}^r &= R_s i_{ds}^r + \frac{d}{dt} \lambda_{ds}^r - \omega_r \lambda_{qs}^r \text{ and,} \\ v_{qs}^r &= R_s i_{qs}^r + \frac{d}{dt} \lambda_{qs}^r + \omega_r \lambda_{ds}^r. \end{aligned} \quad (2)$$

$$R_s(T_{sw}) = R_{s20}(1 + \alpha(T_{sw} - 20^\circ\text{C})). \quad (3)$$

The HF model in (4) is derived from (2) under assumptions that the angular injection frequency (ω_h) is much higher than the electrical rotating speed (ω_r) and the coupled inductances are sufficiently small to be neglected compared to self-inductances. Specifically, the d -axis HF model was the focus of this study because the HF voltage is injected at the d -axis to minimize the torque ripple [22–29].

$$\begin{aligned} v_{dsh}^r &= R_{dh} i_{dsh}^r + L_{dh} \frac{d}{dt} i_{dsh}^r \text{ and} \\ v_{qsh}^r &= R_{qh} i_{qsh}^r + L_{qh} \frac{d}{dt} i_{qsh}^r. \end{aligned} \quad (4)$$

The equivalent circuit for the d -axis HF model is displayed in Figure 1. This circuit appears simple because it only consists of a HF resistance (R_{dh}) and a HF inductance (L_{dh}) connected in series. In this circuit, the HF resistance contains complicated physical meanings related to losses. This circuit can be redrawn to consider where losses occur, as shown in Figure 1b. Figure 1b comprises R_{sw} and three parallel resistances: R_{stator_core} , R_{rotor_core} , and R_{mag} . In this circuit, a stator winding resistance (R_{sw}) represents the conduction losses. The core loss at the stator core and rotor core (P_{L_core}) and the magnet loss (P_{L_mag}) are

represented by R_{stator_core} , R_{rotor_core} , and R_{mag} in (5). These losses occur due to voltage variations (v_{dm}), which are induced by HF flux variations caused by the HF voltage injection. These two losses are represented as equivalent resistances R_{series_core} and R_{series_mag} in (6). Figure 1c shows the equivalent circuit with R_{series_core} , R_{series_mag} , and R_{dh}' , as defined in (7).

$$P_{L_core} = \frac{v_{dm}^2}{R_{core|stator}} + \frac{v_{dm}^2}{R_{core|rotor}}. \tag{5}$$

$$P_{L_mag} = \frac{v_{dm}^2}{R_{mag}}.$$

$$R_{series_core}(T_{mag}) = \frac{P_{L_core}(T_{mag})}{i_{dsh}^2}. \tag{6}$$

$$R_{series_mag}(T_{mag}) = \frac{P_{L_mag}(T_{mag})}{i_{dsh}^2}.$$

$$R_{dh}'(T_{mag}) = R_{series_core}(T_{mag}) + R_{series_mag}(T_{mag}). \tag{7}$$

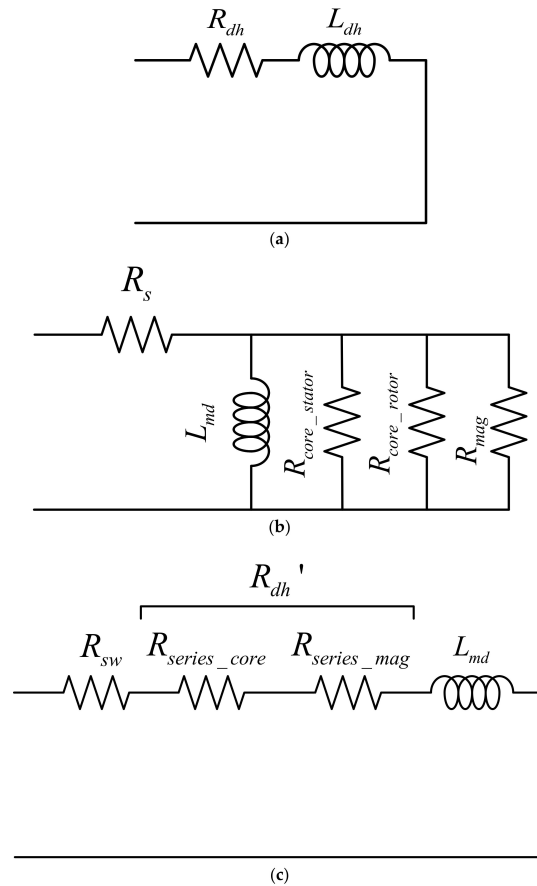


Figure 1. D-axis HF impedance model. (a) Series impedance model of d -axis HF equivalent circuit. (b) Parallel impedance model of d -axis HF equivalent circuit. (c) Series impedance model considering where losses occur.

Based on this analysis, the extracted HF resistance from the signal injection (R_{dh}) is equivalent to the summation of R_{sw} and R_{dh}' in (8), as shown in Figure 1c. The magnet temperature estimation based on the HF resistance utilized the R_{series_mag} variations with magnet temperature. Therefore, R_{series_mag} should be decoupled from the other resistive components to estimate the magnet temperature.

$$R_{dh}(T_s, T_{mag}) = R_{sw}(T_{sw}) + R_{dh}'(T_{mag}). \tag{8}$$

To decouple the other components, R_{stw} and R_{series_core} should be identified. The stator resistance (R_{stw}) is compensated by measuring the stator winding temperature. As a result, the stator winding dependency is removed and R_{dh}' in (8) is obtained, which is only affected by magnet temperature. In R_{dh}' , R_{series_core} and R_{series_mag} should be separated. However, the identification of R_{series_core} from (8) is difficult compared with R_{stw} . Hence, for the estimation, variations in R_{series_mag} with magnet temperature should be dominant in R_{dh}' . However, the permanent magnets in motors are normally segmented to reduce magnet losses related to R_{series_mag} . Therefore, it should be experimentally confirmed whether the magnet temperature can be determined by the HF resistance.

The d -axis HF inductance is derived by using dynamic permeance (P_d) and the winding function (N_a), which are described in (9). Permeance consists of even-order harmonics because the N pole has an identical geometrical structure to the S pole. Moreover, the harmonic of a winding function is constant because a winding function represents a winding configuration. In contrast, permeance is affected by dynamic permeability, as defined in (10), which is determined by the core saturation level. The core saturation is affected by the magnet temperature because the residual flux density (B_r) of a magnet varies according to the magnet temperature in (1).

$$P_d(\phi_e, \theta_r) = \left(P_{d0} + \sum_{k=1}^{\infty} P_{d2k} \cos(2k(\phi_e - \theta_r)) \right) \text{ and} \tag{9}$$

$$N_a(\phi_m) = \sum_{h=1}^{\infty} N_h \cos(h\phi_m).$$

$$\mu_{dd} = \frac{\partial B}{\partial H} = \frac{B_h}{H_h}. \tag{10}$$

$$L_{dh} = L_{Is} + \frac{3}{2} \pi P_{d0} \left(N_1^2 + \sum_{k=1}^{\infty} N_{3k+1}^2 + N_{3k-1}^2 \right) + \frac{3}{2} \frac{\pi}{2} P_{d2} N_1^2. \tag{11}$$

Figure 2 shows a concept figure for dynamic permeability variations according to the magnet temperature. The magnet temperature increases from T_1 to T_2 and from T_2 to T_3 and the core is less saturated. The operating point on the B–H curve represented by the blue line moves from $B(T_1)$ to $B(T_2)$ and from $B(T_2)$ to $B(T_3)$. The dynamic permeability increases with increasing magnet temperature as represented by red arrows. The dynamic permeance is proportional to dynamic permeability. As a result, the d -axis HF inductance increases according to increasing magnet temperature because of (11).

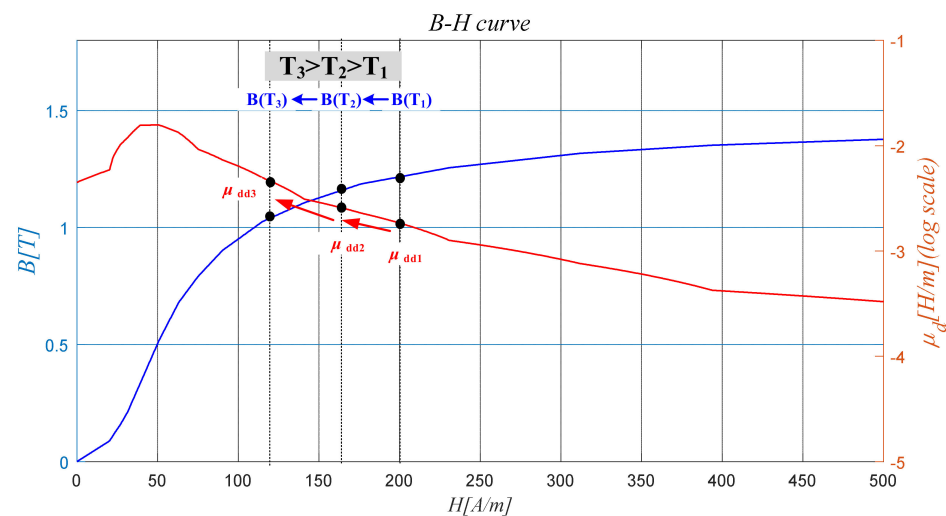


Figure 2. Dynamic permeability variations with magnet temperatures on the B–H curve.

3. Temperature Measurement System

A special rig was designed and developed for conducting the comparative study of the two methods based on HF resistance and HF inductance, as shown in Figure 3. The developed system can measure 9 stator winding temperatures and 32 magnet temperatures simultaneously. The stator winding temperature is measured at nine winding in different slots in A denoted in Figure 3a. Furthermore, the system can measure the magnet temperature at 32 different magnet locations, denoted as the black circles in Figure 3a. As described in Figure 3a, a magnet is segmented into two pieces, denoted as Seg1 and Seg2, which is a typical design for reducing magnet loss.

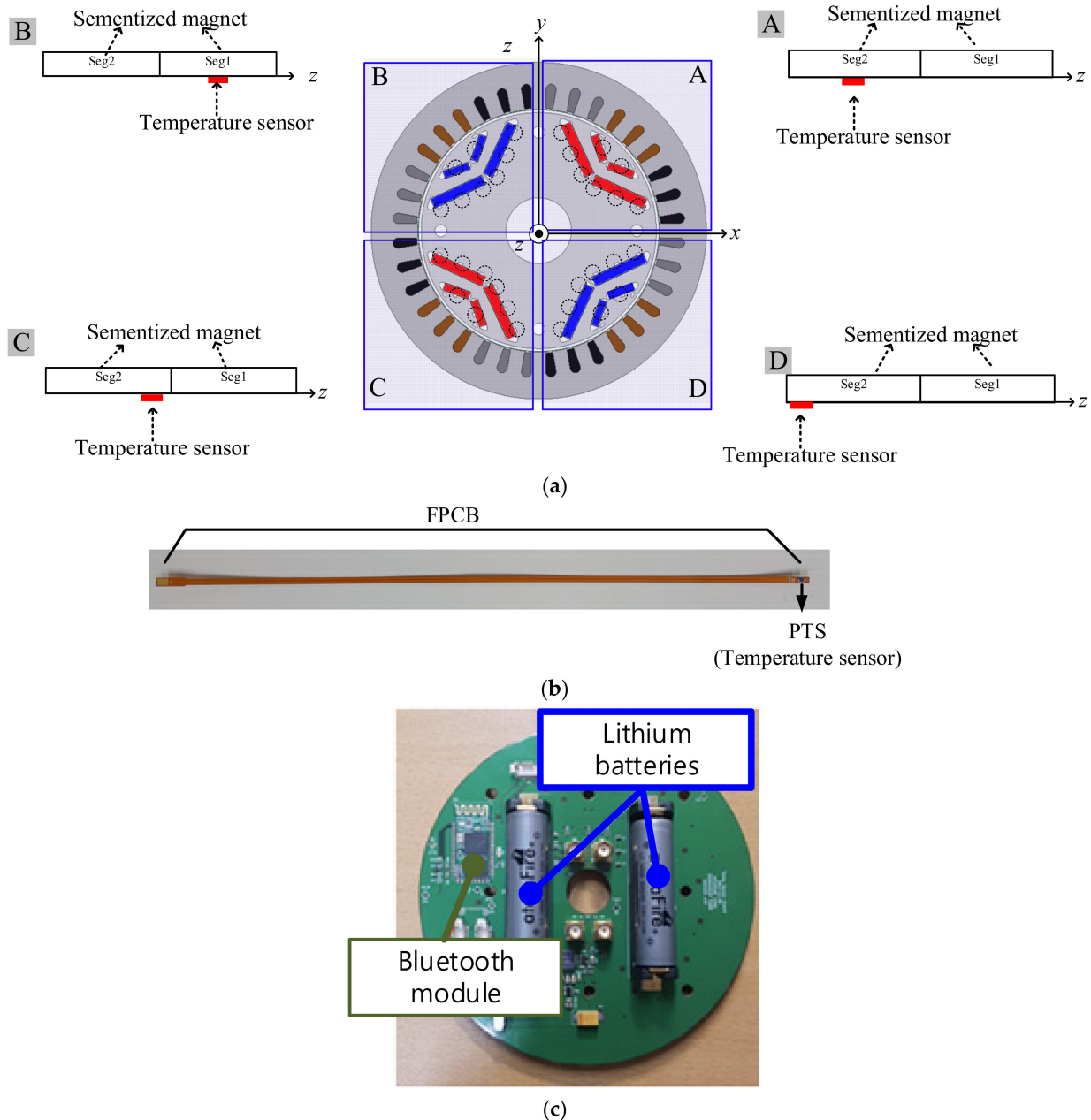


Figure 3. Cont.

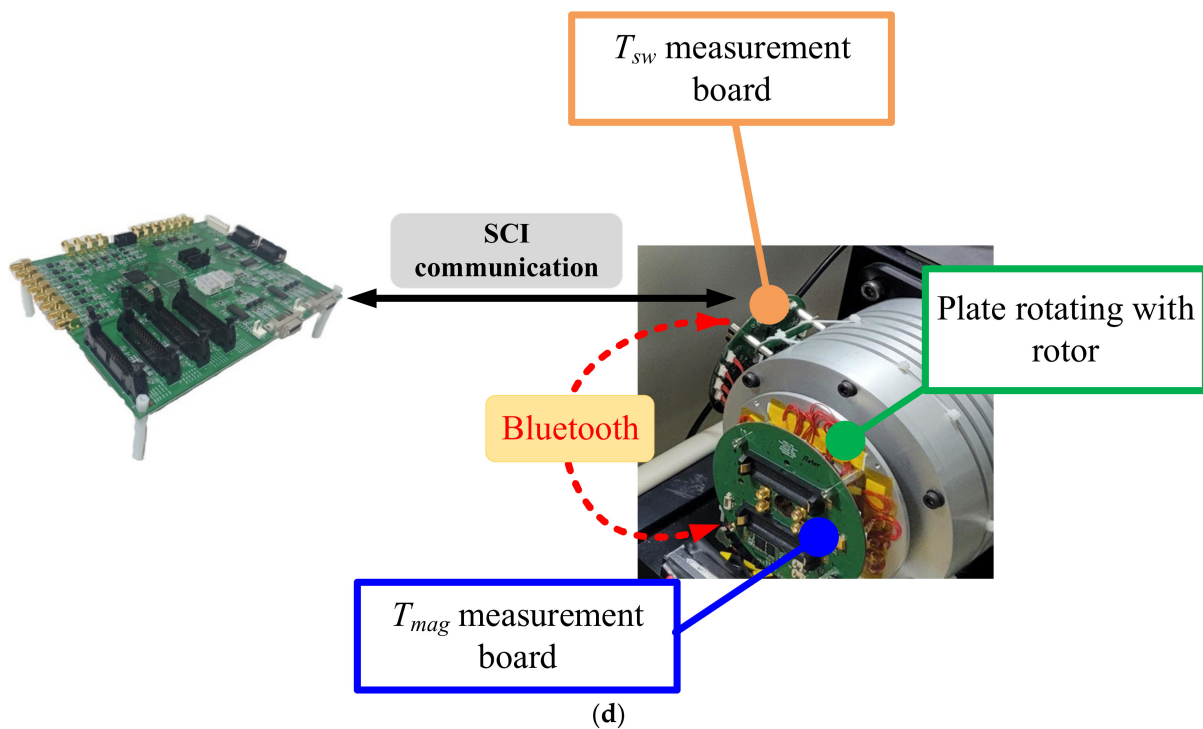


Figure 3. Special rig for magnet temperature. (a) Cross-section of the developed motor. (b) Sensor board. (c) Measurement board. (d) Developed motor with a measurement system.

As shown in Figure 3a, the temperature sensors were placed in small holes to measure the magnet temperature, which acted similarly to flux barriers (i.e., air gaps). Hence, the size and location of the holes were selected to make the flux variations negligible. These holes were placed considering the flux variations and the size of the hole was designed to be as small as possible (1 mm × 2 mm). The manufactured IPMSM parameters are listed in Table 1.

Table 1. Parameters of IPMSM.

Parameter	Value
Poles	4
Rated torque	10 N·m
Rated speed at 310 V	1800 r/min

The sensor board was manufactured using a flexible printed circuit board (FPCB), and a platinum temperature sensor (PTS), sized 0.85 mm × 1.55 mm, was selected as the sensor to be placed on the board, as shown in Figure 3b. Its error is bounded by approximately ±1.1 °C, ranging from −50 to +150 °C. The sensor line goes to the hole in the shaft. Then, through a hollow shaft, the sensor line is connected to the measurement board on the special plate, as shown in Figure 3c. This plate rotates with the rotor as shown in Figure 3d.

Figure 3c shows a measurement board. Two measurement boards are employed to measure the magnet and stator winding temperatures, as shown in Figure 3d. Moreover, the measurement boards are powered by batteries, as shown in Figure 3c, and were connected to the sensor boards in Figure 3b to measure the temperatures. The board on the plate in Figure 3d measures the magnet temperature, which is transmitted to the measurement board on the stationary side via Bluetooth. The board on the stationary side receives magnet temperature from the board on the special plate and connects to the temperature sensors on stator windings. This board measures the stator winding temperature using temperature sensors on stator windings. Finally, the board on the stationary side transfers

the gathered magnet and stator winding temperatures to the main control board through SCI communication. The specifications of the measurement board are provided in Table 2.

Table 2. Specifications of temperature measurement system.

Parameter	Value
ADC	16 channels 12-bit resolution
Wireless Transmission	Bluetooth
Temperature Sensor Class	F0.3
Battery Capacity	3.7 V 900 mAh 2 cells
Operating Temperature	−20 to +65 °C with Li-ion battery −20 to +125 °C with LiSOCL ₂ battery

4. Comparison of Two Methods Based on Experiment Results

Figure 4 shows the overall experimental setup, which includes a control board, an inverter, and a target motor in a motor and generator set. In this setup, the HF resistance and HF inductance were obtained based on the magnet temperature to compare two methods of HF resistance-based and HF inductance-based estimations. After the comparison, the most appropriate estimation method was determined.

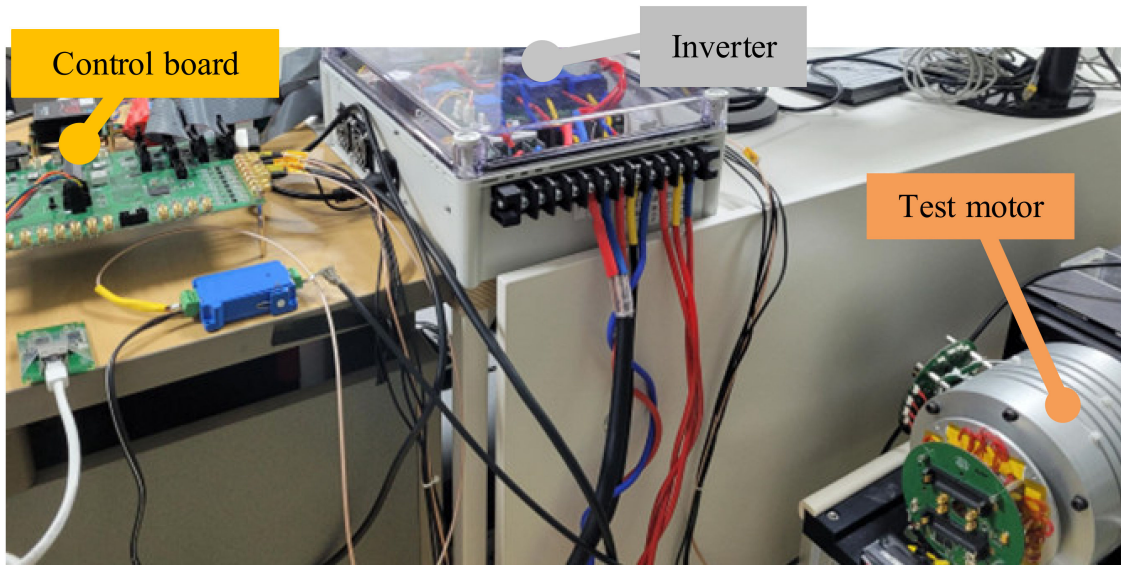


Figure 4. Overall experimental setup, including a control board, an inverter, and the developed special rig.

For the HF signal injection, the nonlinearity effect of the inverter in Figure 5 should be compensated. The nonlinearity effect δV_{xs} is defined in (12), where v_{xn}^* and v_{xn} are the x -phase pole voltage’s reference and x -phase pole voltage synthesized by the inverter, respectively. The inverter nonlinearity effect can be approximated by an arctangent function in (13) [30]. The result is shown in Figure 5, where “Arctan” refers to the approximation function in (13) for the nonlinearity compensation. The approximation error between δV_{xs} and “Arctan” is denoted by the yellow line, which is negligible, as shown in Figure 5.

$$\delta V_{xs} = v_{xs}^* - v_{xs}^r, \text{ where } x \in \{a, b, c\}. \tag{12}$$

$$\delta V_{xs} = \frac{2V_{\text{sat}}k_{xt}}{\pi} \cdot \text{atan}(K_{\text{atan}} \cdot i_{xs}). \tag{13}$$

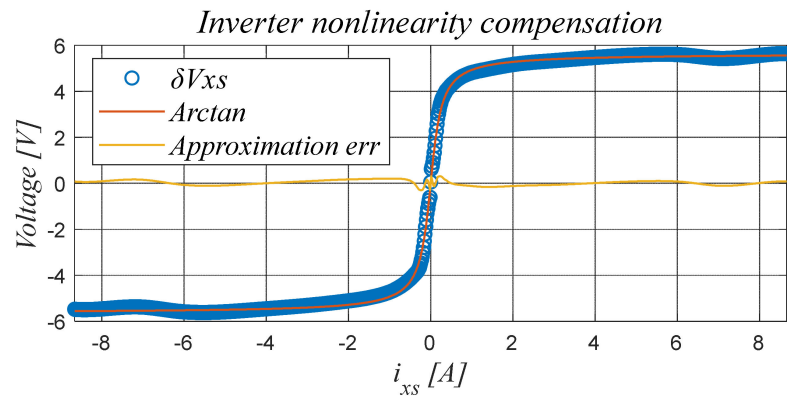


Figure 5. Inverter nonlinearity effect.

Figure 6 describes the extraction process for HF resistance and HF inductance. As depicted in Figure 6, the stator winding and magnet temperatures were measured by the developed rig. In addition, the communication methods between the boards are clearly highlighted. In the red-colored box in this block diagram, the HF voltage (v_{dqsh}^r) was injected into the rotor reference frame. In the blue-colored box, the injection frequency component (i_{dqsh}^r) in the measured current $i_{dqsh_sen}^r$ was extracted by a band pass filter (BPF) with a cut-off frequency set as the injection frequency. The feedback current (i_{dqsh}^r) for current control was obtained by decoupling the injection current (i_{dqsh}^r) from the measured current ($i_{dqsh_sen}^r$), as shown in the blue colored box. Through this process, the HF impedance (i.e., the HF resistance and HF inductance) could be extracted, as shown in the green colored box without any current controller interference. In this process, the measurement delay, including digital delay and PWM delay, was considered as twice the sampling time.

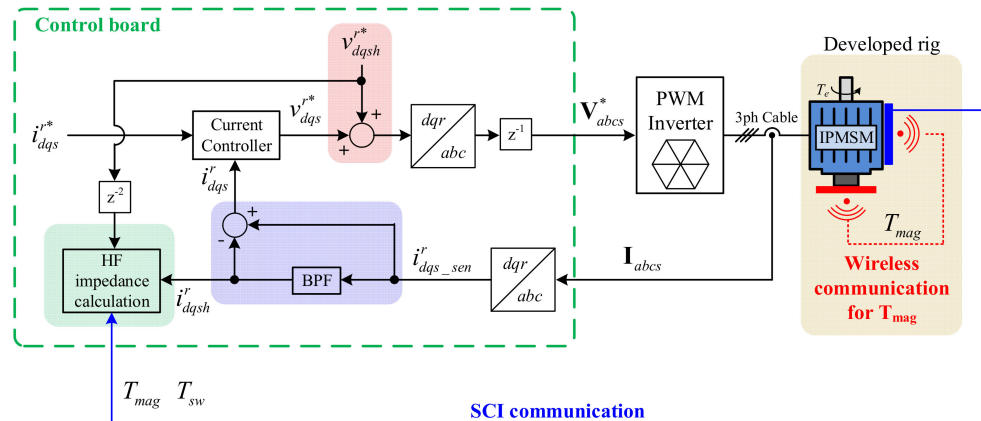


Figure 6. HF resistance and HF inductance extraction process, where a reference value is denoted by a superscript of *.

The injection voltage (v_{dqsh}^r) is given in (14). The injection voltage magnitude V_h was 30 V and the angular injection frequency was $2\pi 500$ Hz. The induced d -axis current is represented as (15), and its current magnitude and phase are given by (16). The impedance magnitude and phase were calculated, as shown in Figure 7a,b. The measured magnet temperature and stator winding temperature are shown in Figure 7c,d. In this figure, the torque ranged from 0 N·m to the rated torque of 10 N·m, and the speed ranged from 300 to 900 r/min. The magnet temperature varied from -24.5 to $+82$ °C. In these ranges, the HF impedance was secured at 300 operating points (5 speeds \times 10 torques \times 6 temperatures) and plotted in Figure 7. Based on the measured data in Figure 7, the comparison result at low speed is described in Section 4.1. Moreover, the possibility of applying the standstill condition is discussed in Section 4.2.

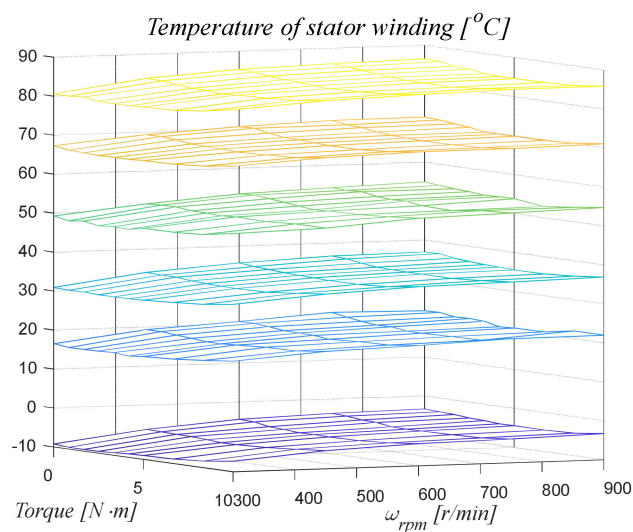
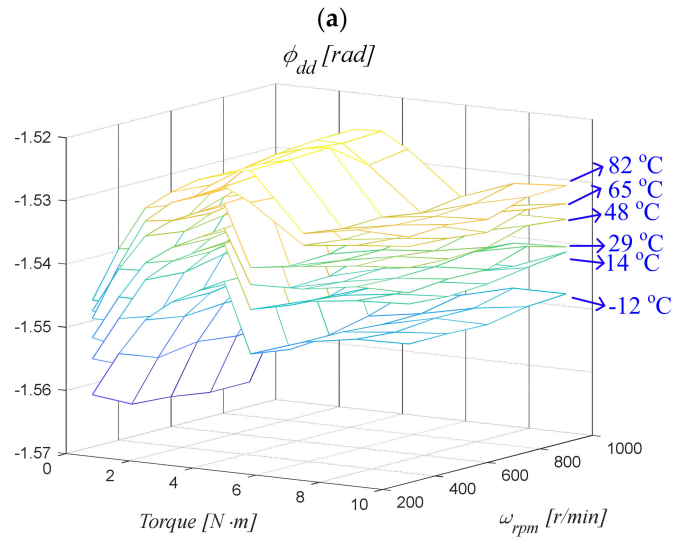
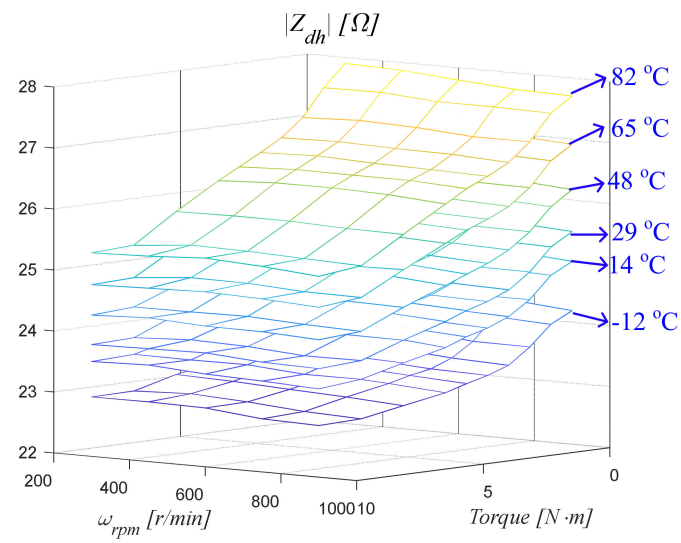


Figure 7. Cont.

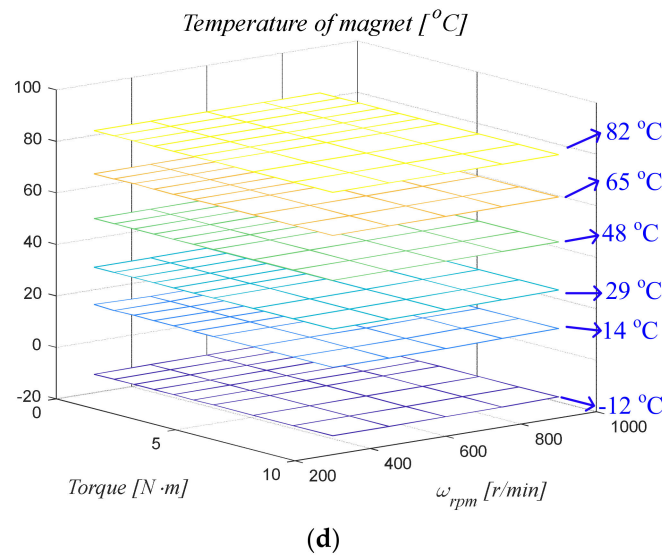


Figure 7. Experimental results. (a) Magnitude of HF impedance ($|Z_{dh}|$), (b) phase of HF impedance (ϕ_{dd}), (c) stator winding temperature (T_{sw}), and (d) magnet temperature (T_{mag}).

$$v_{dqsh}^{r*} = \begin{bmatrix} V_h \cos(\omega_h t) \\ 0 \end{bmatrix}. \tag{14}$$

$$i_{ddsh}^r = |i_{ddsh}^r| \cos(\omega_h t + \phi_{dd}). \tag{15}$$

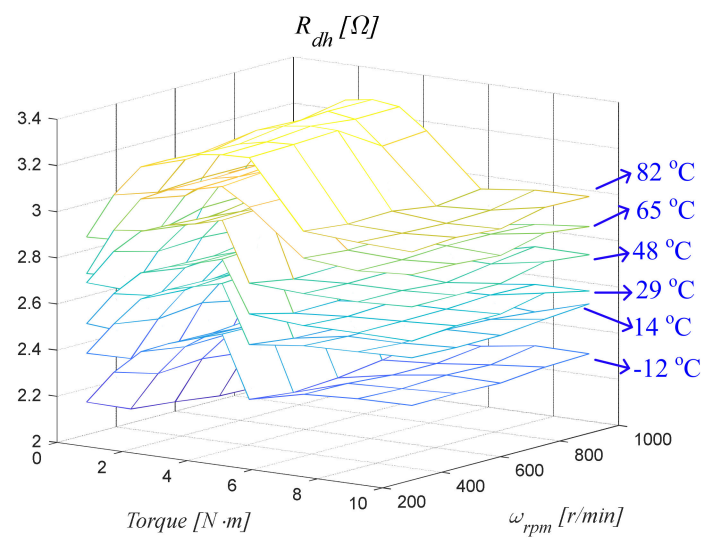
$$|i_{ddsh}^r| = \left| \frac{V_h}{\sqrt{R_{dh}^2 + \omega_h^2 L_{dh}^2}} \right| \text{ and } \phi_{dd} = -\tan^{-1} \left(\frac{\omega_h L_{dh}}{R_{dh}} \right). \tag{16}$$

4.1. Comparison of Two HF Signal Injection Methods at Low Speed

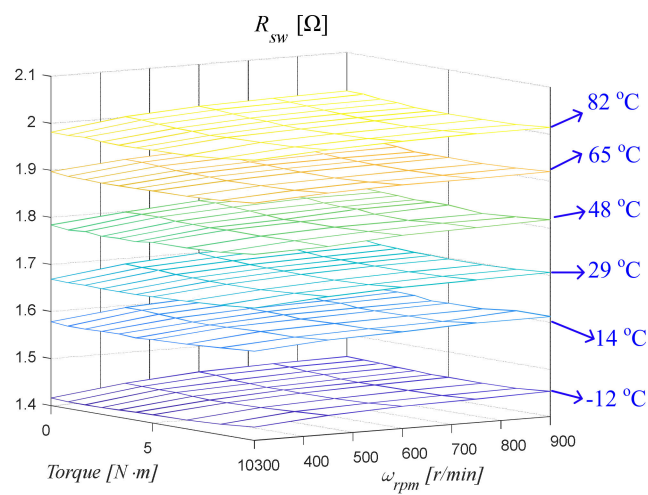
The HF resistance was calculated using (17) and shown in Figure 8a. Figure 8b shows stator winding resistance. As shown in Figure 8, six data sets were located according to the following magnet temperatures: $-12\text{ }^\circ\text{C}$, $+14\text{ }^\circ\text{C}$, $+29\text{ }^\circ\text{C}$, $+48\text{ }^\circ\text{C}$, $+65\text{ }^\circ\text{C}$, and $+82\text{ }^\circ\text{C}$. For example, the data set of R_{dh} with $82\text{ }^\circ\text{C}$ is a group of HF resistances according to the speeds and torques when the magnet temperature was about $82\text{ }^\circ\text{C}$. According to Figure 8, six data sets of R_{dh} in (8) were distributed according to the magnet temperature.

$$R_{dh} = \frac{V_h}{|i_{ddsh}^r|} \cos(\phi_{dd}). \tag{17}$$

Figure 9 shows R_{dh}' in (7), which is the HF resistance decoupled with R_{sw} by using the measured stator winding temperature in (3). As shown in Figure 9, the six data sets of R_{dh}' were overlapped or crossed over. In other words, R_{dh}' was not distributed according to the magnet temperature. This experimental result indicates that HF resistance was not appropriate for estimating magnet temperature in the experimental setup.

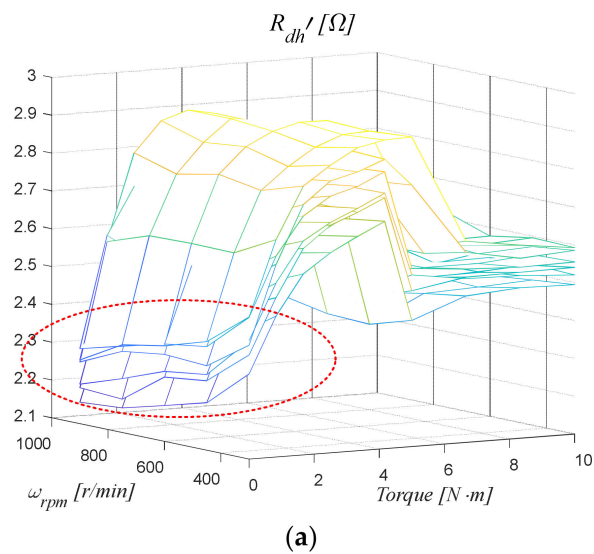


(a)



(b)

Figure 8. Resistive components (a) HF resistance (R_{dh}) and (b) stator winding resistance (R_{sw}).



(a)

Figure 9. Cont.

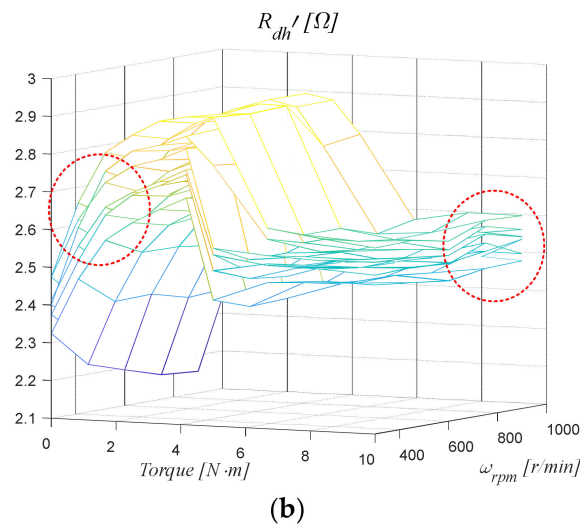


Figure 9. HF resistance R_{dh}' . (a) R_{dh}' and (b) another side view of (a).

D -axis HF inductance was calculated by (18) and plotted in Figure 10, where six datasets of L_{dh} are plotted at $T_{mag} = \{-12\text{ }^\circ\text{C}, +14\text{ }^\circ\text{C}, +29\text{ }^\circ\text{C}, +48\text{ }^\circ\text{C}, +65\text{ }^\circ\text{C}, +82\text{ }^\circ\text{C}\}$. The HF inductance was consistent without any overlapping or crossing over. In other words, the HF inductance increased when the magnet temperature increased. To clarify this correlation, the HF inductance was normalized using (19) and shown in Figure 11. The normalized HF inductance ($L_{dh.Norm}$) was well distributed according to the magnet temperature. An analysis clearly indicated that the HF inductance had a strong correlation with the magnet temperature. Accordingly, the estimation method based on HF inductance was expected to achieve significantly better performance than the method based on HF resistance.

$$L_{dh} = -\frac{V_h}{\omega_h |i_{ddsh}^r|} \sin(\phi_{dd}). \tag{18}$$

$$L_{dh.Norm} = \frac{L_{dh} - \text{MIN}(L_{dh})}{\text{MAX}(L_{dh}) - \text{MIN}(L_{dh})}. \tag{19}$$

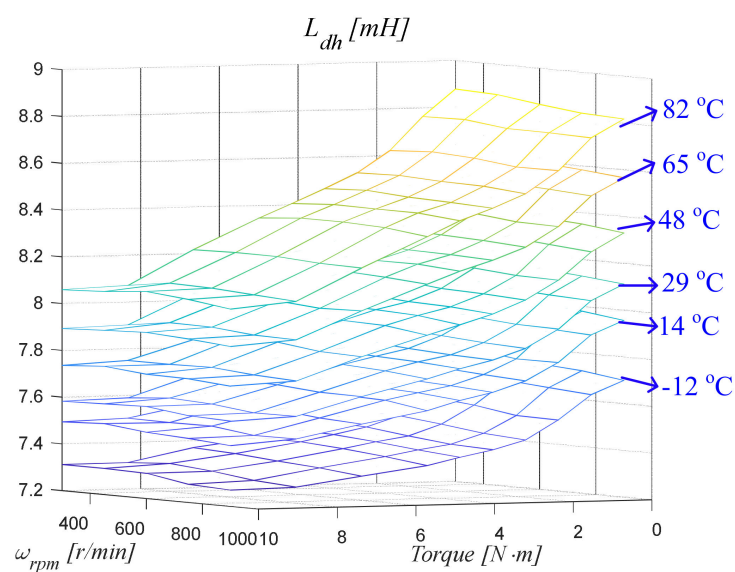


Figure 10. HF inductance L_{dh} .

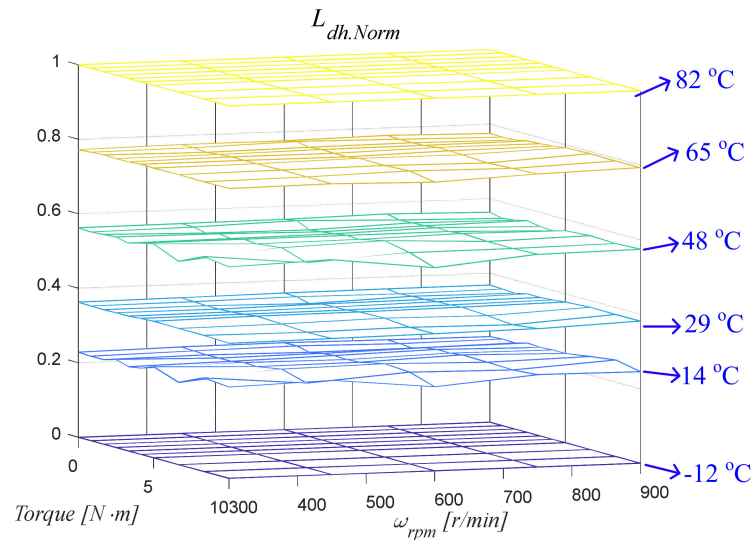


Figure 11. Normalized HF inductance $L_{dh.Norm}$.

The sensitivity of the HF inductance $S(L_{dh})$ can be calculated using (20) and was in the range of 0.12 to 0.16%/°C. The sensitivity was larger than the absolute value of α_{mag} (approximately 0.1%/°C) in (1). This means that HF inductance is sensitive enough to be used in the magnet temperature estimation.

$$S(L_{dh}) = \frac{L_{dh}(T_{mag}) - L_{dh}(20\text{ °C})}{T_{mag} - 20\text{ °C}} \frac{100}{L_{dh}(20\text{ °C})} \text{ [%/ °C]}. \quad (20)$$

The HF inductance (L_{dh}) can be approximated by a second-order polynomial with T_{mag} in (21). The approximation’s determinant coefficient (R^2) in (22) was greater than approximately 0.99 in all the tested load conditions. Therefore, this approximation was very accurate and was convenient for implementing the estimation method.

$$L_{dh_app}(T_e, \omega_{rpm}, T_{mag}) = A(T_e, \omega_{rpm}) \times T_{mag}^2 + B(T_e, \omega_{rpm}) \times T_{mag} + C(T_e, \omega_{rpm}). \quad (21)$$

$$R^2 = \frac{\sum_{k=1}^n \left(L_{dh_app}(i) - \frac{1}{n} \sum_{k=1}^n L_{dh_mea}(i) \right)^2}{\sum_{k=1}^n \left(L_{dh_mea}(i) - \frac{1}{n} \sum_{k=1}^n L_{dh_mea}(i) \right)^2}. \quad (22)$$

4.2. Comparison of Two HF Signal Injection Methods at a Standstill

In [14,26], HF signal injection methods were applied to conduct estimations in the standstill condition. In this subsection, it will be discussed whether both methods could be applied to the standstill condition and which method was more appropriate based on the measured HF impedance and temperature.

Figure 12 shows the d -axis HF impedance magnitude ($|Z_{dh}|$) and phase (ϕ_{dd}) according to the rotor angle under a standstill with the no-load condition. As shown in Figure 12, the mechanical rotor angle (θ_{rm}) was changed from 0° to 179° with a step of 1°. The electrical rotor angle ranged from 0°E to 358°E with a step of 2°E, where E is an abbreviation of electrical because the motor was a four-pole machine. The magnet temperature changed from −10 °C to +81 °C. The d -axis HF inductance was measured at 3240 points (180 rotor positions × 18 magnet temperatures), with the results presented in Figure 12.

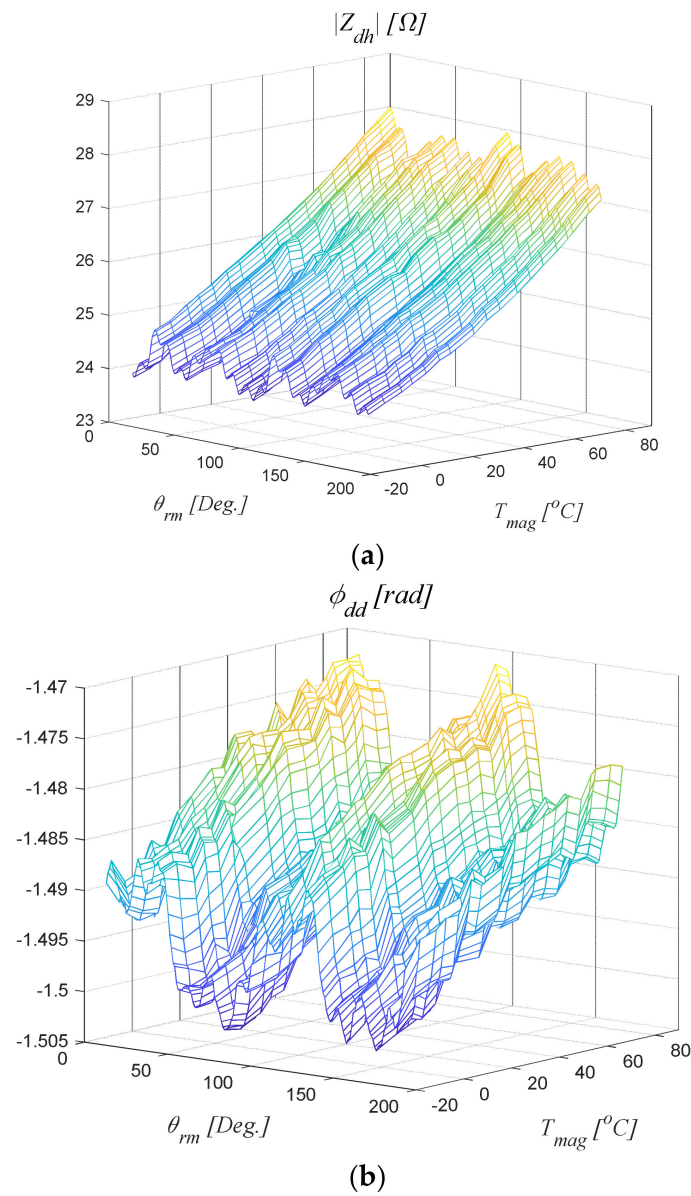


Figure 12. HF impedance (a) magnitude ($|Z_{dh}|$) and (b) phase (ϕ_{dd}).

Figure 12 shows that spatial harmonics are included in the HF impedance, rendering the application of the estimation method based on HF injection difficult. Therefore, spatial harmonics should be considered in the estimation [26]. Similarly, as noted in [26], spatial harmonics could be considered and removed by the process in (23). The term L_{dh_Del} refers to the inductance variation according to the magnet temperature without spatial harmonics. This experimental result is shown in Figure 13a. In this figure, the HF inductance increased with increasing magnet temperature, which indicates that L_{dh_Del} could be utilized to estimate the magnet temperature.

$$L_{dh_Del}(T_{mag}) = L_{dh_SS}(\theta_r, T_{mag}) - \frac{1}{n} \sum_{k=1}^n L_{dh_SS}(\theta_r, T_{mag}(k)). \quad (23)$$

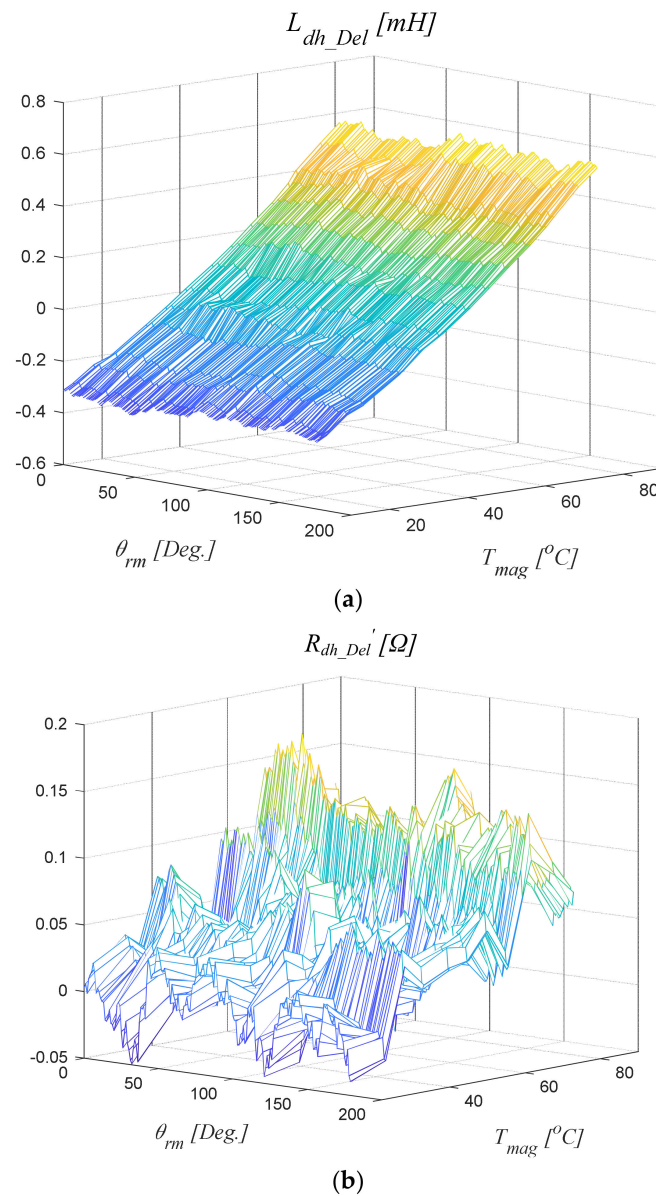


Figure 13. HF impedance after decoupling the spatial harmonics. (a) L_{dh_Del} and (b) R_{dh_Del}' .

The same process could also be applied to the high-frequency resistance without R_{sw} (R_{dh}') in (24). The obtained R_{dh_Del}' in (24) denoted HF resistance variations with the magnet temperature after decoupling the spatial harmonics. As shown in Figure 13b, the relationship between HF resistance without R_{sw} and T_{mag} was unclear. For example, when the magnet temperature increased, HF resistance increased and decreased according to the magnet temperature and rotor angle. In other words, variations in HF resistance were inconsistent with magnet temperature variations. Therefore, the HF resistance was difficult to apply for estimations at standstill. These comparisons suggested that the HF inductance-based method was significantly better for estimations at standstill.

$$R_{dh_Del}'(T_{mag}) = R_{dh}'(\theta_r, T_{mag}) - \frac{1}{n} \sum_{k=1}^n R_{dh}'(\theta_r, T_{mag}(k)). \quad (24)$$

In conclusion, the HF resistance had an unclear correlation with the magnet temperature. This was because the magnet was segmented and the magnet losses were minimized, resulting in R_{serise_mag} not being dominant in R_{dh}' . Furthermore, the HF resistance-based estimation method required measuring the stator winding temperature to remove the stator

winding resistance as described in (7) and (8). Moreover, the HF inductance was strongly correlated with the magnet temperature and this method did not require any additional temperature sensors, unlike the HF resistance-based method. Based on the experimental results, the HF inductance-based method was more appropriate for estimating the magnet temperature compared to the HF resistance-based method in this experimental setup.

5. Conclusions

The focus of this paper was estimating magnet temperature at low speeds. Specifically, magnet temperature estimation methods based on HF resistance and HF inductance were compared and the more appropriate method for estimating magnet temperature at low speeds was determined. For the comparison, a special rig was developed in which the magnet and stator winding temperatures could be measured. In this setup, HF resistance and HF inductance datasets were obtained according to speed, torque, and magnet temperature. Based on these experimental results, the HF inductance was more strongly correlated with the magnet temperature compared to the HF resistance. Additionally, the possibility of applying two methods at standstill was discussed based on the experimental results. In this comparison, spatial harmonics were considered. The comparison results indicated that HF inductance had a stronger correlation with magnet temperature compared to HF resistance at standstill. Accordingly, the HF inductance-based estimation method is expected to achieve better performance under low speed and standstill conditions. Furthermore, the HF inductance-based method does not require any temperature sensors, unlike the HF resistance-based method.

Author Contributions: Conceptualization, H.-S.J.; methodology, H.-S.J.; writing—original draft, H.-S.J.; supervision, H.-S.J.; investigation, H.K.; Software, S.-G.K. and J.-J.J.; writing—review and editing, H.K., S.-G.K., J.-J.J. and H.-S.J. All authors have read and agreed to the published version of the manuscript.

Funding: This work was supported by the Korea Institute of Energy Technology Evaluation and Planning (KETEP) and the Ministry of Trade, Industry & Energy (MOTIE) of the Republic of Korea (No. 20223A10100020), the Dongguk University Research Fund of 2020, and the National Research Foundation of Korea (NRF) grant funded by the Korea government (MSIT) (No. 2022R1A4A1031885).

Data Availability Statement: Not applicable.

Acknowledgments: The authors are thankful to human resources development project of the Korea Institute of Energy Technology Evaluation and Planning (KETEP) for the support grant funded by the Korea government Ministry of Trade, Industry and Energy under the project titled: “Middle market enterprise specialized human resources development for residential and commercial fuel cell”, numbered: 20224000000580.

Conflicts of Interest: The authors declare no conflict of interest.

References

1. Calin, M.; Helerea, E. Temperature influence on magnetic characteristics of NdFeB permanent magnets. In Proceedings of the 2011 7TH International Symposium on Advanced Topics in Electrical Engineering (ATEE), Bucharest, Romania, 12–14 May 2011; pp. 1–6.
2. Li, S.; Sarlioglu, B.; Jurkovic, S.; Patel, N.R.; Savagian, P. Analysis of Temperature Effects on Performance of Interior Permanent Magnet Machines for High Variable Temperature Applications. *IEEE Trans. Ind. Appl.* **2017**, *53*, 4923–4933. [[CrossRef](#)]
3. Kim, Y.; Sul, S. Torque Control Strategy of an IPMSM Considering the Flux Variation of the Permanent Magnet. In Proceedings of the 2007 IEEE Industry Applications Annual Meeting, New Orleans, LA, USA, 23–27 September 2007; pp. 1301–1307.
4. Sebastian, T. Temperature effects on torque production and efficiency of PM motors using NdFeB magnets. *IEEE Trans. Ind. Appl.* **1995**, *31*, 353–357. [[CrossRef](#)]
5. Ruoho, S.; Kolehmainen, J.; Ikaheimo, J.; Arkkio, A. Interdependence of Demagnetization, Loading, and Temperature Rise in a Permanent-Magnet Synchronous Motor. *IEEE Trans. Magn.* **2010**, *46*, 949–953. [[CrossRef](#)]
6. Park, D.; Jung, H.; Cho, H.; Sul, S. Design of Wireless Temperature Monitoring System for Measurement of Magnet Temperature of IPMSM. In Proceedings of the 2018 IEEE Transportation Electrification Conference and Expo (ITEC), Long Beach, CA, USA, 13–15 June 2018; pp. 656–661.
7. Mellor, P.H.; Roberts, D.; Turner, D.R. Lumped parameter thermal model for electrical machines of TEFC design. *IEEE Proc. B—Electr. Power Appl.* **1991**, *138*, 205–218. [[CrossRef](#)]

8. Demetriades, G.D.; De La Parra, H.Z.; Andersson, E.; Olsson, H. A Real-Time Thermal Model of a Permanent-Magnet Synchronous Motor. *IEEE Trans. Power Electron.* **2010**, *25*, 463–474. [[CrossRef](#)]
9. Huber, T.; Peters, W.; Böcker, J. Monitoring critical temperatures in permanent magnet synchronous motors using low-order thermal models. In Proceedings of the 2014 International Power Electronics Conference (IPEC-Hiroshima 2014—ECCE ASIA), Hiroshima, Japan, 18–21 May 2014; pp. 1508–1515.
10. Kral, C.; Haumer, A.; Bin Lee, S. A practical thermal model for the estimation of permanent magnet and stator winding temperatures. *IEEE Trans. Power Electron.* **2014**, *29*, 455–464. [[CrossRef](#)]
11. Specht, A.; Böcker, J. Observer for the rotor temperature of IPMSM. In Proceedings of the 14th International Power Electronics and Motion Control Conference EPE-PEMC 2010, Ohrid, Republic of Macedonia, 6–8 September 2010; pp. T4-12–T4-15.
12. Specht, A.; Wallscheid, O.; Böcker, J. Determination of rotor temperature for an interior permanent magnet synchronous machine using a precise flux observer. In Proceedings of the 2014 International Power Electronics Conference (IPEC-Hiroshima 2014—ECCE ASIA), Hiroshima, Japan, 18–21 May 2014; pp. 1501–1507.
13. Wallscheid, O.; Specht, A.; Böcker, J. Observing the Permanent-Magnet Temperature of Synchronous Motors Based on Electrical Fundamental Wave Model Quantities. *IEEE Trans. Indust. Electron.* **2017**, *64*, 3921–3929. [[CrossRef](#)]
14. Reigosa, D.; Fernandez, D.; Tanimoto, T.; Kato, T.; Briz, F. Comparative analysis of BEMF and pulsating high-frequency current injection methods for PM temperature estimation in PMSMs. *IEEE Trans. Power Electron.* **2017**, *32*, 3691–3699. [[CrossRef](#)]
15. Feng, G.; Lai, C.; Tjong, J.; Kar, N.C. Noninvasive Kalman Filter Based Permanent Magnet Temperature Estimation for Permanent Magnet Synchronous Machines. *IEEE Trans. Power Electron.* **2018**, *33*, 10673–10682. [[CrossRef](#)]
16. Jung, H.-S.; Kim, H.G.; Sul, S.K.; Berry, D.J. Magnet Temperature Estimation of IPMSM by Using Reactive Energy. In Proceedings of the 2019 10th International Conference on Power Electronics and ECCE Asia (ICPE 2019—ECCE Asia), Busan, Republic of Korea, 27–30 May 2019; pp. 1–6.
17. Jung, H.-S.; Kim, H.; Sul, S.K.; Berry, D.J. Temperature Estimation of IPMSM by Using Fundamental Reactive Energy Considering Variation of Inductances. *IEEE Trans. Power Electron.* **2021**, *36*, 5771–5783. [[CrossRef](#)]
18. Jung, H.-S.; Kim, H.; Sul, S.K.; Berry, D.J. Permanent Magnet Temperature Estimation in a Mass-Produced Traction Motor for an Electric Vehicle. *IEEE Trans. Transp. Electrification.* **2022**, *8*, 1863–1873. [[CrossRef](#)]
19. Jung, H.-S.; Young, O.D. Estimation of Stator and Magnet Temperatures of IPMSM from Active and Reactive Energies at Medium and High Speeds. *IEEE Trans. Transp. Electrification.* **2022**. [[CrossRef](#)]
20. Ganchev, M.; Kral, C.; Wolbank, T. Sensitivity and robustness aspects of sensorless rotor temperature estimation technique for permanent magnet synchronous motor. In Proceedings of the 2012 15th International Power Electronics and Motion Control Conference (EPE/PEMC), Novi Sad, Serbia, 4–6 September 2012; pp. LS3a-L1.2-1–LS3a-L1.2-6.
21. Ganchev, M.; Kral, C.; Wolbank, T. Sensorless rotor temperature estimation of permanent magnet synchronous motor under load conditions. In Proceedings of the IECON 2012—38th Annual Conference on IEEE Industrial Electronics Society, Montreal, QC, Canada, 25–28 October 2012; pp. 1999–2004.
22. Reigosa, D.D.; Briz, F.; Garcia, P.; Guerrero, J.M.; Degner, M.W. Magnet temperature estimation in surface PM machines using high-frequency signal injection. *IEEE Trans. Ind. Appl.* **2010**, *46*, 1468–1475. [[CrossRef](#)]
23. Reigosa, D.D.; Fernandez, D.; Yoshida, H.; Kato, T.; Briz, F. Permanent-magnet temperature estimation in PMSMs using pulsating high-frequency current injection. *IEEE Trans. Ind. Appl.* **2015**, *51*, 3159–3168. [[CrossRef](#)]
24. Jung, H.-S.; Park, D.; Kim, H.; Sul, S.; Berry, D.J. Noninvasive Magnet Temperature Estimation in IPMSM by High Frequency Pulsating Sinusoidal Voltage Injection. In Proceedings of the 2018 IEEE Transportation Electrification Conference and Expo (ITEC), Long Beach, CA, USA, 13–15 June 2018; pp. 858–862.
25. Jung, H.-S.; Park, D.H.; Kim, H.; Sul, S.K.; Berry, D.J. Noninvasive Magnet Temperature Estimation in IPMSM by Using High Frequency Inductance with Pulsating High Frequency Voltage Signal Injection. *IEEE Trans. Ind. Appl.* **2019**, *55*, 3076–3086. [[CrossRef](#)]
26. Jung, H.-S.; Kim, H.; Sul, S.K.; Berry, D.J. Magnet Temperature Estimation of Traction Motor in Standstill with Considering Spatial Harmonics. *IEEE Trans. Ind. Electron.* **2021**, *68*, 10546–10557. [[CrossRef](#)]
27. Kim, H.; Jung, H.-S.; Sul, S.K. Stator Winding Temperature Estimation of IPMSM Based on a High-frequency Voltage Signal Injection. In Proceedings of the 2020 IEEE Transportation Electrification Conference & Expo (ITEC), Chicago, IL, USA, 23–26 June 2020; pp. 896–900.
28. Kim, H.; Jung, H.-S.; Sul, S.K. Stator Winding Temperature and Magnet Temperature Estimation of IPMSM Based on High-Frequency Voltage Signal Injection. *IEEE Trans. Ind. Electron.* **2023**, *70*, 2296–2306. [[CrossRef](#)]
29. Reigosa, D.; Fernández, D.; Martínez, M.; Guerrero, J.M.; Diez, A.B.; Briz, F. Magnet Temperature Estimation in Permanent Magnet Synchronous Machines Using the High Frequency Inductance. *IEEE Trans. Ind. Appl.* **2019**, *55*, 2750–2757. [[CrossRef](#)]
30. Kim, D.W.; Kwon, Y.C.; Sul, S.K.; Kim, J.H.; Yu, R.S. Suppression of injection voltage disturbance for high-frequency square-wave injection sensorless drive with regulation of induced high-frequency current ripple. *IEEE Trans. Ind. Appl.* **2019**, *52*, 302–312. [[CrossRef](#)]

Disclaimer/Publisher’s Note: The statements, opinions and data contained in all publications are solely those of the individual author(s) and contributor(s) and not of MDPI and/or the editor(s). MDPI and/or the editor(s) disclaim responsibility for any injury to people or property resulting from any ideas, methods, instructions or products referred to in the content.